RSC Advances

PAPER

View Article Online
View Journal | View Issue

Cite this: *RSC Adv.*, 2019, **9**, 17885

Mott variable-range hopping transport in a MoS_2 nanoflake†

Jianhong Xue,[a] Shaoyun Huang,*[a] Ji-Yin Wang[a] and H. Q. Xu*[abcd]

The transport characteristics of a disordered, multilayered MoS_2 nanoflake in the insulator regime are studied by electrical and magnetotransport measurements. The MoS_2 nanoflake is exfoliated from a bulk MoS_2 crystal and the conductance G and magnetoresistance are measured in a four-probe setup over a wide range of temperatures. At high temperatures, we observe that ln G exhibits a $-T^{-1}$ temperature dependence and the transport in the nanoflake dominantly arises from thermal activation. At low temperatures, where the transport in the nanoflake dominantly takes place *via* variable-range hopping (VRH) processes, we observe that ln G exhibits a $-T^{-1/3}$ temperature dependence, an evidence for the two-dimensional (2D) Mott VRH transport. Furthermore, we observe that the measured low-field magnetoresistance of the nanoflake in the insulator regime exhibits a quadratic magnetic field dependence $\sim \alpha B^2$ with $\alpha \sim T^{-1}$, fully consistent with the 2D Mott VRH transport in the nanoflake.

Received 27th April 2019
Accepted 28th May 2019

DOI: 10.1039/c9ra03150b

rsc.li/rsc-advances

Despite the rapid developments in MoS_2 layered materials and device applications, the nature of charge transport still remains elusive, since the experimentally measured carrier mobility in the materials is significantly lower than theoretical prediction.[1–4] Disorders, such as sulphur vacancies, charge impurities, surface absorbents, charged traps at MoS_2 layer–substrate interfaces,[5–8] *etc.*, strongly influence the transport properties of the layered MoS_2 materials. Generally, in a disordered system,[9] transport can be divided into two different regimes, separated by the mobility edge E_C. Tuning the Fermi energy E_F across the mobility edge causes a metal–insulator transition[10–12] from extended to localized states or *vice versa*. In the insulating regime, where carriers are all frozen to localized states at energies below the mobility edge E_C at zero temperature, carrier transport can take place *via* thermal activation at relatively high temperatures and *via* variable-range hopping (VRH) at low but finite temperatures. When the carrier transport is predominantly due to thermal activation, the conductance (G) exhibits a temperature (T) dependence of $\ln G \sim -T^{-1}$ and, thus, the characteristics activation energy E_a can be extracted from the Arrhenius plot of the measured conductance G as a function of temperature T. When temperature goes higher than a critical value (~100 K in many compound semiconductor materials), phonon scattering can become significantly strong, leading to a characteristic temperature dependence that the conductance decreases with increasing temperature. At low temperatures, the current is carried *via* VRH processes in which a localized electron at the Fermi level moves to another localized state in an optimum hopping distance. The optimum distance is determined by the tradeoff between the lowest energy differences and the shortest hopping distances. In a noninteracting d-dimensional system, the density of states N_F at the Fermi level is finite and the conductance can be well described by the Mott VRH mechanism[13] with $\ln G \sim -T^{-p}$ where exponent $p = 1/(d+1)$. Pollak,[14,15] Efros and Shklovskii[16] pointed out that a soft gap can be opened up at the Fermi level by taking into account the long range electron–electron Coulomb interactions. The density of states at the Fermi level thus vanishes and the conductance should be described by the so called ES VRH mechanism[17–19] with exponent $p = 1/2$ in $\ln G \sim -T^{-p}$, independent of the dimension.

Due to the two-dimensional (2D) nature and the natural presence of disorders, layered MoS_2 offers a renewed platform to investigate VRH mechanisms of 2D transport. Thermally activated transport,[20] and nearest neighbor hopping (NNH) and VRH transport[5–8,21–24] have been observed and discussed in many recent experimental studies of disorders, layered MoS_2. Wu *et al.*,[5] Ghatak *et al.*[7] and Jariwala *et al.*[8] studied the transport properties of atomically thin layer MoS_2 devices and found that the transport in the MoS_2 layers are well described by the 2D Mott VRH mechanism over a wide range of temperatures T (300–30 K). Qiu *et al.*[6] examined the transport properties of few-layer MoS_2 devices at low carrier densities and found that 2D Mott VRH mechanism dominate only the transport in the MoS_2

[a]*Beijing Key Laboratory of Quantum Devices, Key Laboratory for the Physics and Chemistry of Nanodevices, Department of Electronics, Peking University, Beijing 100871, China. E-mail: hqxu@pku.edu.cn; syhuang@pku.edu.cn*

[b]*Beijing Academy of Quantum Information Sciences, West Bld. #3, No. 10 Xibeiwang East Rd., Haidian District, Beijing 100193, China*

[c]*Beijing Academy of Quantum Information Sciences, Beijing 100193, China*

[d]*NanoLund, Division of Solid State Physics, Lund University, Box 118, S-221 00 Lund, Sweden*

† Electronic supplementary information (ESI) available. See DOI: 10.1039/c9ra03150b

layer in a low T region (100–20 K), while in the high T region (300–100 K) NNH dominates the transport in the layers. Liang *et al.*[24] found a similar transition between NNH and VRH while the corresponding transition temperature is 70 K. Lo *et al.*[21] studied transport in a monolayer MoS_2 nanoflake and found that both the Mott and the ES VRH models can provide satisfactory explanation for their measurements at $T < 190$ K. Very recently, Kim *et al.*[22] and Papadopoulos *et al.*[23] studied transport in few-layered nanoflakes of *n*-butyllithium treated polymorphic MoS_2. While Kim *et al.*[22] found that their transport measurements are described by the 2D Mott VRH mechanism, Papadopoulos *et al.*[23] showed contradictorily that the transport in their few-layered MoS_2 nanoflakes is well described by the ES VRH mechanism. In all the above mentioned works, the temperature-dependent measurements of the conductance or the resistance are exclusively analyzed to determine transport mechanisms. Beside some controversies are present in assignment of VRH transport mechanisms, no carrier density dependent transition between different transport mechanisms was reported in these works.

Magnetotransport measurements could also be used to distinguish the two VRH mechanisms in the disordered MoS_2 layers. In a common situation where the magnetoresistance shows a quadratic dependence on magnetic field as αB^2, the coefficient α has different temperature dependences for the two VRH transport mechanisms.[25] In the Mott VRH regime the coefficient $\alpha \propto T^{-3/(d+1)}$, whereas in the ES VRH regime the coefficient $\alpha \propto T^{-3/2}$. Thus, magnetotransport measurements could be analyzed together with the temperature and carrier density dependent measurements to identify the transport mechanisms in disordered MoS_2 nanoflakes. We notice that although there are some works[26] reporting the magnetoresistance of MoS_2, no efforts to distinguish between the Mott and ES VRH transports based on magnetotransport measurements has been made yet.

In this work, we report on an experimental study of the transport characteristics of a disordered MoS_2 nanoflake by electrical and magnetotransport measurements in a four-probe setup over a temperature range of 6 to 300 K and at different carrier densities. The study is focused on the insulator regime where the Fermi energy E_F lies below the mobility edge E_C. When E_F is tuned close to E_C, the characteristics of thermally activated transport and phonon scattering are observed in the conductance measurements of the nanoflake. When E_F is tuned far below E_C, the measured ln G shows a $-T^{-1}$ dependence at relatively high temperatures and a $-T^{-1/3}$ dependence at relatively low temperatures. A good quadratics magnetic field dependence $\sim \alpha B^2$ of the magnetoresistance is also observed in the nanoflake and a T^{-1} dependence of coefficient α is extracted. These electrical and magnetotransport measurements provide a solid evidence that the Mott VRH rather than ES VRH transport is the dominant transport mechanism in our disordered MoS_2 nanoflake in the insulating regime at low temperatures.

The MoS_2 nanoflakes studied in this work are obtained by exfoliation from a commercially available bulk MoS_2 crystal. The exfoliated MoS_2 nanoflakes are transferred onto a highly doped silicon substrate covered with a 300 nm-thick layer of SiO_2 on top. Electrical contacts are prepared using electron-beam lithography (EBL) for pattern definition, electron-beam evaporation for deposition of 5 nm-thick titanium and 50 nm-thick gold, and lift-off process. Fig. 1(a) shows an atomic force microscope (AFM) image of a fabricated device measured for this work and the schematic for the measurement circuit setup. The MoS_2 nanoflake in the device has a width of $W \sim 400$ nm and a thickness of $t \sim 10$ nm, see the AFM line scan measurements across an edge of the nanoflake shown in the lower panel of Fig. 1(a). The device consists of four metal stripe contacts, which we labeled as contacts 1 to 4 as in Fig. 1(a). These contacts have a width of 200 nm. The edge-to-edge distances between contacts 1 and 2, between contacts 2 and 3, and between contacts 3 and 4 are 80, 450 and 100 nm, respectively. The measurements are performed in a Physical Property Measurement System (PPMS) cryostat, which provides temperatures in a range of 300 to 2 K and magnetic fields up to 9 Tesla. The four-probe setup is adopted in the measurements, in order to exclude the contact resistances, in which a source–drain bias voltage V_{ds} is applied between contacts 1 and 4, the channel current I_{ds} and the voltage drop (V_{23}) between contacts 2 and 3 are simultaneously recorded, see the circuit setup in Fig. 1(a). The Fermi level E_F in the nanoflake is modulated by a voltage V_g applied to the silicon substrate (back gate).

Fig. 1(b) shows the measured channel current I_{ds} as a function of the voltage drop V_{23} between contacts 2 and 3 for the device shown in Fig. 1(a) at a fixed back gate voltage of $V_g = -30$ V and different temperatures. It is seen in the figure that the measured I_{ds}–V_{23} curves are straight lines. The good linearity is found in all the measured I_{ds}–V_{23} curves over a wide range of back gate voltages and of temperatures, which ensures that the transport characteristics of the MoS_2 channel are extracted from the measurements. Fig. 1(c) shows the measured channel conductance $G = I_{ds}/V_{23}$ as a function of back gate voltage V_g at different temperatures. It is seen that the device is a typical n-type transistor. The channel conductance shows very different temperature dependence at high back gate voltages (on the right side of point A) and at low back gate voltages (on the left side of point A), where the crossover point A is located at $V_g \sim -30$ V, as indicated by a black arrow in Fig. 1(c). At the high back gate voltages (on the right side of point A), the conductance G is increased with decreasing temperature and then becomes decreased with further lowering temperature. At the low back gate voltages (on the left side of point A), however, the conductance G is monotonously decreased with decreasing temperature in the entire measured temperature range (from 300 to 6 K). The observed temperature dependence of the conductance at low temperatures indicates that the MoS_2 channel is in the insulating regime and the Fermi energy E_F lies below the mobility edge E_C throughout the entire measurement range of back gate voltages. The characteristic conductance increase with decreasing temperature observed at high back gate voltages and high temperatures arises from the interplay between the thermal activation transport and phonon scattering. This interplay phenomena could be better visualized by plotting the resistance R_{23} as a function of temperature

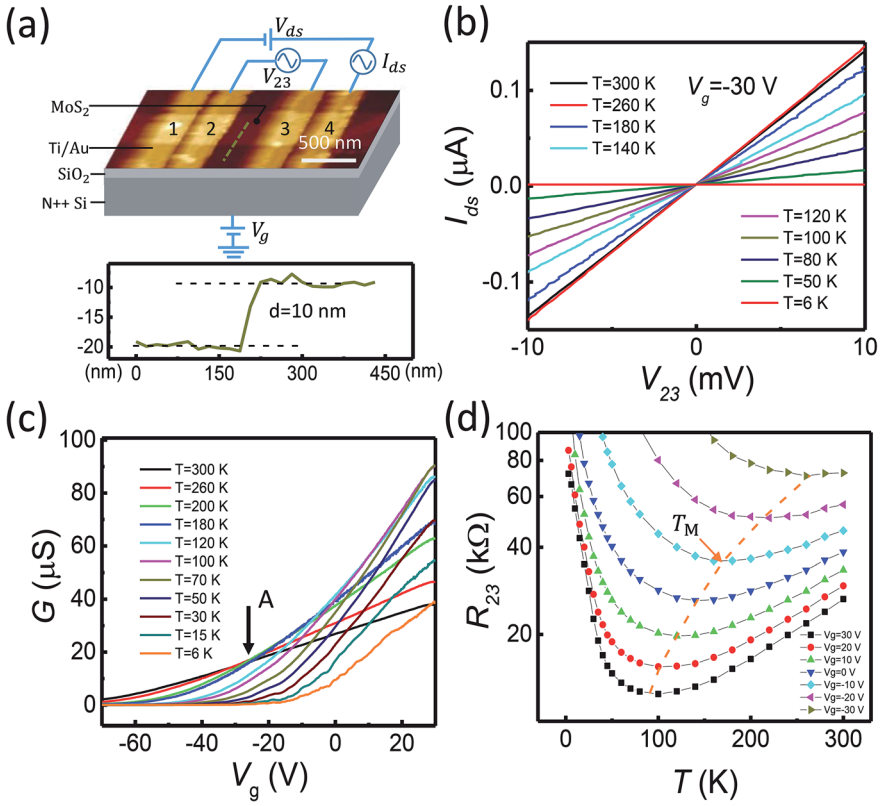

Fig. 1 (a) AFM image of the MoS_2 nanoflake device and schematic view of the device layer structure and measurement setup (top panel), and height profile measured using AFM along the dashed line in the AFM image (bottom panel). Here it is shown that the MoS_2 nanoflake in the device has a thickness of 10 nm. (b) Source–drain current I_{ds} *vs.* voltage V_{23} measured for the device at temperatures from 6 to 300 K and at back gate voltage $V_g = -30$ V. (c) Transfer characteristics of the field-effect device at temperatures from 6 to 300 K. (d) Resistance of the nanoflake plotted against temperature T at different back gate voltages. T_M marks the temperature position at which the resistance has a minimum in the curve measured at each back gate voltage. The dashed line connecting the values of T_M at different back gate voltages is the guide to the eyes.

measured at different back gate voltages as shown in Fig. 1(d). Here, we can clearly recognize that at a given high back gate voltage $V_g > -30$ V, there exists a characteristic temperature T_M, at which the resistance has a minimum. Apparently, T_M increases with decreasing back gate voltage, see the yellow dashed line in Fig. 1(d), and can reach a temperature as low as ~100 K at $V_g = 30$ V. Physically, at such a high back gate voltage, the Fermi level E_F is close to the mobility edge E_C and a significant number of carriers can be excited to the extended states located at energies above the mobility edge at high temperatures. Thus, at $T > T_M$, the observed fact that the resistance decreases with decreasing temperature is mainly due to reduction in phonon scattering with decreasing temperature. However, at $T < T_M$, the phonon scattering becomes less important and the resistance becomes closely related to the number of carriers which are thermally excited to the extended states. As the back gate voltage V_g decreases, the Fermi level E_F is gradually moved away from the mobility edge E_C, leading to an increase in T_M as seen in Fig. 1(d).

Fig. 2 shows the Arrhenius plot of the measured conductance as a function of temperature at different back gate voltages. In the temperature region of 80 K < T < T_M, *i.e.*, the shaded part except for the upper-left corner region in the figure, relatively large thermal kinetic energy assisted transport dominates and the temperature dependence of the conductance can be well modelled by the thermally activated transport[20] as $G_a = G_0 e^{-E_a/k_B T}$. Here, G_0 is the conductance at the high temperature limit, $E_a = (E_C - E_F)$ is the activation energy, and k_B is the Boltzmann constant. The extracted activation energy E_a is shown in the inset of Fig. 2 as a function of the back gate voltage. The activation energy E_a decreases linearly with increasing V_g from −70 to −30 V and turns to saturate with further increasing V_g to the positive side, in good agreement with the fact that the Fermi level moves closer to the mobility edge with increasing back gate voltage.

However, the thermally activated transport model does not describe the measurements in the low temperature region [the right, unshaded part of Fig. 2] as seen from the deviations from the fitting lines in the region. Physically, in this low temperature region, VRH conduction becomes dominant and is responsible for the temperature dependent characteristics of the measured conductance. In theory, the conductance in VRH mechanisms can be described as

$$G = G_0 e^{-\left(\frac{T_p}{T}\right)^p}, \quad (1)$$

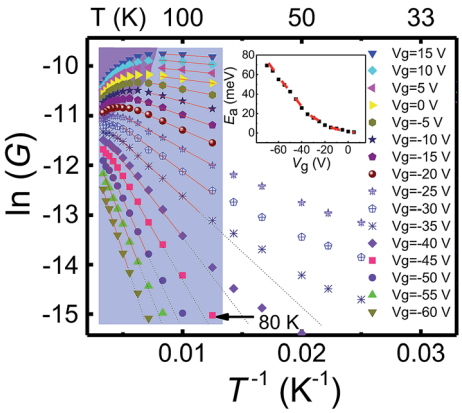

Fig. 2 ln G plotted against T^{-1} (inverse of temperature) for the device at different back gate voltages. The region on the left marked by grey color is for the measurements at temperatures higher than ~80 K, at which the transport in the nanoflake is well described by the thermal activation mechanism. The upper-left corner marked by light purple color is the region of the measurements at high temperatures and high positive gate voltages, where the characteristics of phonon scattering in the layered MoS_2 is observed. Lines in the grey colored region are straight line fits to the measured data. The inset shows the extracted activation energy E_a from the straight line fits in the grey color region as a function of back gate voltage V_g. The red dashed line in the inset is a guide to the eyes to clarify the change of E_a.

where T_p is the characteristic temperature and the exponent p depends on VRH mechanism. For the Mott VRH conduction, the exponent p is dimension dependent and has a value of $p = 1/3$ in a 2D system. For the ES VRH conduction, the exponent is dimension independent and has a value of $p = 1/2$. To identify whether the Mott VRH mechanism or the ES VRH mechanism play a dominant role in determining the transport characteristics of the MoS_2 nanoflake, we plot the measured conductance as a function of $T^{-1/2}$ and of $T^{-1/3}$ in Fig. 3(a) and (b), respectively. It is seen in Fig. 3(a) that the measured data cannot be fitted by straight lines, indicating that the ES VRH mechanism does not describe the transport behavior of the nanoflake in this low temperature range. However, in Fig. 3(b), straight-line fits agree excellently with the measured data over the entire temperature range of 6 to 80 K. Thus, the transport in the MoS_2 nanoflake in this temperature range is most likely governed by the 2D Mott VRH process. We have also checked and fitted our data against the 3D Mott VRH model (see ESI†), in which the exponent takes a value of $p = 1/4$, and found large deviations, indicating that the transport in the nanoflake should be of the 2D nature. The 2D nature of the transport in our nanoflake is also supported by the angular dependent magnetoresistance measurements as shown in ESI.†

Employing the 2D Mott VRH mechanism, we can further analyze the temperature dependence of the conductance to extract the characteristic temperature $T_{1/3}$ and localization length ξ_{loc} in the nanoflake at different gate voltages V_g. The results are shown in the inset of Fig. 3(b). It is seen that $T_{1/3}$ monotonically decreases from $\sim 10^5$ to $\sim 10^2$ K with increasing V_g from −70 to 5 V. Theoretically, $T_{1/3}$ is related to the localization length as $T_{1/3} = 13.8/(k_B N_F \xi_{loc}^2)$, where N_F is the density of states at Fermi level. The N_F can be determined from the gate voltage dependence of the activation energy E_a by taking into account the quantum capacitance C_d as[12,27]

$$\frac{dE_F}{dV_g} = -\frac{dE_a}{dV_g} = \frac{eC_g}{C_g + C_d}, \quad (2)$$

with $C_d = e^2 N_F$. Here, C_g is the unit area capacitance and can be obtained from $C_g = \frac{\varepsilon_0 \varepsilon}{d}$ with ε_0 being the vacuum permittivity, ε and d being the dielectric constant and layer thickness of SiO_2. The calculated values of C_d and N_F are from 6 to 10 μF cm^{-2} and from 3.75 to 6.25 × 10^{13} eV^{-1} cm^{-2}, respectively. Thus, the derived localization length of the nanoflake is found to increase from 3.4 to 33.7 nm with increasing V_g from −70 to 5 V, as shown in the inset of Fig. 3(b).

Fig. 4(a) show the magnetoresistance characteristics at different temperatures in the 2D VRH transport regime at V_g = −20 V with the magnetic field B applied perpendicular to the MoS_2 nanoflake. Here, the MoS_2 nanoflake is in the x–y

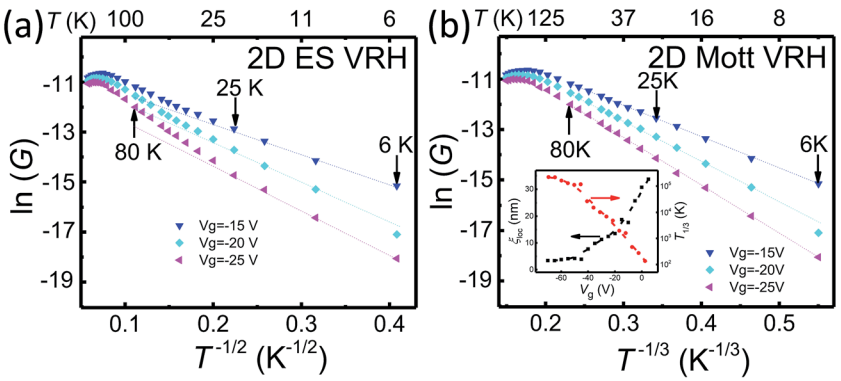

Fig. 3 (a) ln G plotted against $T^{-1/2}$ for the device measured at different back gate voltages. Lines are straight line (2D ES VRH theory) fits to the measurement data at low temperatures. Clearly, the straight line fits do not describe the measurement data at temperatures of 25 to 80 K. (b) The same as in (a) but plotted against $T^{-1/3}$. Lines are straight line (2D Mott VRH theory) fits to the measurement data at temperatures of 6 to 80 K. Here, excellent fits are obtained over this range of temperatures. The inset shows the extracted characteristic temperature $T_{1/3}$ and localization length ξ_{loc} as a function of back gate voltage V_g for the MoS_2 nanoflake based on the 2D Mott VRH theory.

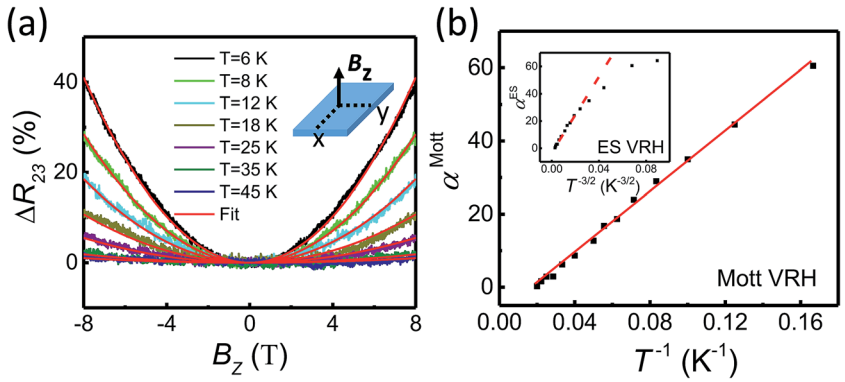

Fig. 4 (a) Magnetoresistance as a function of magnetic field B_z applied perpendicular to the MoS_2 nanoflake plane (as shown in the inset) measured at back gate voltage $V_g = -20$ V and at different temperatures. Red solid lines are fits to the measured data based on the wave-function shrinkage model. (b) Prefactor α^{Mott} as a function of T^{-1} extracted from the measured magnetoresistance curves at different temperatures T. The red solid line presents the predicted values of α^{Mott} by the wave-function shrinkage model in the Mott VRH regime. The inset shows the prefactor α^{ES} extracted from the same magnetoresistance measurements as a function of $T^{-3/2}$. The dashed line in the inset shows the results that would be predicted by the wave-function shrinkage model in the ES VRH regime.

plane, the current flow is along the x axial direction, and the magnetoresistance is defined as $\Delta R_{23} = [R(B) - R(B = 0)]/R(B = 0)$. Clearly, the magnetoresistance shows a positive quadratic dependence on magnetic field B at temperatures below ~50 K. In the wave-function shrinkage model,[28–31] the positive quadratic magnetoresistance is attributed to the contraction of the electronic wave function at traps in a magnetic field, thus leading to a reduction of hopping probability. Quantitatively, in the wave-function shrinkage model, the magnetoresistance in the Mott VRH regime can be expressed as[25]

$$\Delta R_{23} = 0.0893\left[\frac{e^2\xi_{loc}{}^4}{36\hbar^2}\right]\left(\frac{T_{Mott}}{T}\right)B^2 = \alpha^{Mott}B^2, \quad (3)$$

where T_{Mott} is a characteristic temperature, $\hbar$ is the reduced Planck constant and the prefactor α^{Mott} is proportional to T^{-1}. Note that in the ES VRH regime, the magnetoresistance can be found by replacing (T_{Mott}/T) in eqn (3) with $(T_{ES}/T)^{3/2}$. Thus, the magnetoresistance also shows a positive quadratic magnetic field dependence, but the prefactor α^{ES} is proportional to $T^{-3/2}$ instead of T^{-1}. We fit the positive quadratic magnetoresistance curves at different temperatures in Fig. 4(a) based on the wave-function shrinkage models in both the Mott VRH and the ES VRH regime. The derived prefactors α^{Mott} and α^{ES} are shown in Fig. 4(b). Clearly, the extracted α^{ES} as a function of $T^{-3/2}$ shown in the inset of Fig. 4(b) exhibits a significant deviation, while the extracted α^{Mott} displays an excellent agreement with the T^{-1} dependence. Thus, the 2D Mott VRH mechanism rather than the ES VRH mechanism is identified for the electron transport in the MoS_2 nanoflake at low temperatures, in good agreement with the analysis shown in Fig. 3.

In conclusion, the transport characteristics of a disordered MoS_2 nanoflake have been investigated in details over a wide range of temperatures in the insulator regime, where the Fermi level E_F in the nanoflake is tuned with use of the back gate voltage to lie below the mobility edge E_C. At relatively high temperatures, the nanoflake exhibits activation transport characteristics. The activation energy $E_a = E_C - E_F$, which measures the energy distance between the mobility edge E_C and the Fermi energy E_F, is extracted in the nanoflake. It is found that the activation energy E_a decreases with increasing back gate voltage at low back gate voltages and turn to saturate towards zero at high back gate voltages. At sufficiently low temperatures, the transport characteristics of the nanoflake are found to be governed by VRH processes. To identify whether the Mott or the ES VRH mechanism plays a dominant role in the system at this low temperature region, the temperature dependent conductance and magnetoresistance have been measured and analyzed. It is found that in this low temperature region the $\ln G$ shows a $-T^{-1/3}$ temperature dependence and the prefactor in the quadratic magnetic field dependent magnetoresistance scales with temperature as T^{-1}. These results provide exclusive evidences that the 2D Mott VRH transport is the dominant transport mechanism at low temperatures in the insulating regime of our disordered MoS_2 nanoflake.

Conflicts of interest

There are no conflicts of interest to declare.

Acknowledgements

This work is supported by the Ministry of Science and Technology of China through the National Key Research and Development Program of China (Grant No. 2017YFA0303304, 2016YFA0300601, 2017YFA0204901, and 2016YFA0300802), the National Natural Science Foundation of China (Grant No. 11874071, 91221202, 91421303, and 11274021), and the Beijing Academy of Quantum Information Sciences (Grant No. Y18G22). HQX also acknowledges financial support from the Swedish Research Council (VR).

References

1 B. Radisavljevic, A. Radenovic, J. Brivio, V. Giacometti and A. Kis, *Nat. Nanotechnol.*, 2011, **6**, 147.
2 Q. H. Wang, K. Kalantar-Zadeh, A. Kis, J. N. Coleman and M. S. Strano, *Nat. Nanotechnol.*, 2012, **7**, 699.
3 Z. Yu, Z.-Y. Ong, S. Li, J.-B. Xu, G. Zhang, Y.-W. Zhang, Y. Shi and X. Wang, *Adv. Funct. Mater.*, 2017, **27**, 1604093.
4 K. Kaasbjerg, K. S. Thygesen and K. W. Jacobsen, *Phys. Rev. B: Condens. Matter Mater. Phys.*, 2012, **85**, 115317.
5 J. Wu, H. Schmidt, K. K. Amara, X. Xu, G. Eda and B. Ozyilmaz, *Nano Lett.*, 2014, **14**, 2730.
6 H. Qiu, T. Xu, Z. Wang, W. Ren, H. Nan, Z. Ni, Q. Chen, S. Yuan, F. Miao, F. Song, G. Long, Y. Shi, L. Sun, J. Wang and X. Wang, *Nat. Commun.*, 2013, **4**, 2642.
7 S. Ghatak, A. N. Pal and A. Ghosh, *ACS Nano*, 2011, **5**, 7707.
8 D. Jariwala, V. K. Sangwan, D. J. Late, J. E. Johns, V. P. Dravid, T. J. Marks, L. J. Lauhon and M. C. Hersam, *Appl. Phys. Lett.*, 2013, **102**, 173107.
9 N. Mott, M. Pepper, S. Pollitt, R. H. Wallis and C. J. Adkins, *Proc. R. Soc. London, Ser. A*, 1975, **345**, 169.
10 B. Radisavljevic and A. Kis, *Nat. Mater.*, 2013, **12**, 815.
11 B. W. Baugher, H. O. Churchill, Y. Yang and P. Jarillo-Herrero, *Nano Lett.*, 2013, **13**, 4212.
12 D. Ovchinnikov, A. Allain, Y. S. Huang, D. Dumcenco and A. Kis, *ACS Nano*, 2014, **8**, 8174.
13 N. F. Mott, *J. Non-Cryst. Solids*, 1968, **1**, 1.
14 M. Pollak, *Discuss. Faraday Soc.*, 1971, **1970**, 13.
15 M. L. Knotek and M. Pollak, *J. Non-Cryst. Solids*, 1972, **8**, 505.
16 A. L. Efros and B. I. Shklovskii, *J. Phys. C: Solid State Phys.*, 1975, **8**, L49.
17 S. I. Khondaker, I. S. Shlimak, J. T. Nicholls, M. Pepper and D. A. Ritchie, *Solid State Commun.*, 1999, **109**, 751.
18 Y. Zhang, P. Dai, M. Levy and M. P. Sarachik, *Phys. Rev. Lett.*, 1990, **64**, 2687.
19 A. Aharony, Y. Zhang and M. P. Sarachik, *Phys. Rev. Lett.*, 1992, **68**, 3900.
20 A. Ayari, E. Cobas, O. Ogundadegbe and M. S. Fuhrer, *J. Appl. Phys.*, 2007, **101**, 014507.
21 S. T. Lo, O. Klochan, C. H. Liu, W. H. Wang, A. R. Hamilton and C. T. Liang, *Nanotechnology*, 2014, **25**, 375201.
22 J. S. Kim, J. Kim, J. Zhao, S. Kim, J. H. Lee, Y. Jin, H. Choi, B. H. Moon, J. J. Bae, Y. H. Lee and S. C. Lim, *ACS Nano*, 2016, **10**, 7500.
23 N. Papadopoulos, G. A. Steele and H. S. J. van der Zant, *Phys. Rev. B*, 2017, **96**, 235436.
24 S. Liang, H. Yang, P. Renucci, B. Tao, P. Laczkowski, S. McMurtry, G. Wang, X. Marie, J. M. George, S. Petit-Watelot, A. Djeffal, S. Mangin, H. Jaffres and Y. Lu, Electrical spin injection and detection in molybdenum disulfide multilayer channel, *Nat. Commun.*, 2017, **8**, 14947.
25 T.-I. Su, C.-R. Wang, S.-T. Lin and R. Rosenbaum, *Phys. Rev. B: Condens. Matter Mater. Phys.*, 2002, **66**, 054438.
26 T.-E. Park, J. Suh, D. Seo, J. Park, D.-Y. Lin, Y.-S. Huang, H.-J. Choi, J. Wu, C. Jang and J. Chang, *Appl. Phys. Lett.*, 2015, **107**, 223107.
27 W. Zhu, T. Low, Y.-H. Lee, H. Wang, D. B. Farmer, J. Kong, F. Xia and P. Avouris, *Nat. Commun.*, 2014, **5**, 3087.
28 F. L. Bloom, W. Wagemans, M. Kemerink and B. Koopmans, *Phys. Rev. Lett.*, 2007, **99**, 257201.
29 Y.-B. Zhou, B.-H. Han, Z.-M. Liao, H.-C. Wu and D.-P. Yu, *Appl. Phys. Lett.*, 2011, **98**, 222502.
30 R. Sadu, N. Haldolaarachchige, D. Chen and D. P. Young, *Appl. Phys. Lett.*, 2013, **102**, 212403.
31 Y. Zhang, H. Ning, Y. Li, Y. Liu and J. Wang, *Appl. Phys. Lett.*, 2016, **108**, 153114.